Composite imaging of auroral forms and convective flows during a substorm cycle

J. Semeter,[1] T. W. Butler,[1] M. Zettergren,[2] C. J. Heinselman,[3] and M. J. Nicolls[3]

Received 25 September 2009; revised 24 February 2010; accepted 25 March 2010; published 14 August 2010.

[1] Measurements obtained with the electronically steerable Poker Flat Incoherent Scatter Radar (PFISR) and collocated all-sky camera were used to construct composite images of ionospheric convective flows and auroral forms during a substorm cycle (onset 26 March 2008, 1146 UT). PFISR was configured to sample an array of 5 × 5 regularly spaced beams on a pulse-by-pulse basis, from which velocity vectors were computed via statistical inversion of groups of beams. Flow fields were resolved at 30 km spatial resolution at 2 min temporal resolution over a 100 × 100 km field and then geographically registered with all-sky imagery recorded at 20 s cadence. An analysis of the composite images has revealed interesting contrasts between growth-, expansion-, and recovery-phase auroras, for example, (1) anticorrelation of ion velocity (electric field) and luminosity (plasma density, hence, conductance) in both space and time during growth phase and expansion phase; (2) identical flow (magnitude and direction) inside and outside the aurora during recovery phase; (3) a large tangential flow component along auroral boundaries during both growth and recovery phase (consistent with electric field directed into the aurora), irrespective of the orientation of the arc boundary; and (4) large relative drift (~2 km/s) between auroral forms and convective flow during recovery phase. These features are interpreted in the context of previous ground-based and space-borne observations. Future PFISR experiments are expected to enable flow field construction at 30 s cadence, which will resolve Alfvén transit time dynamics to putative substorm initiation regions and significantly clarify the observations presented herein.

Citation: Semeter, J., T. W. Butler, M. Zettergren, C. J. Heinselman, and M. J. Nicolls (2010), Composite imaging of auroral forms and convective flows during a substorm cycle, *J. Geophys. Res.*, *115*, A08308, doi:10.1029/2009JA014931.

1. Introduction

[2] The term "substorm" was introduced by *Akasofu* [1964] to describe episodic intensifications and expansions of the auroral oval. As the range of phenomena connected to theses events grew, a more physical definition was sought. The term now embodies a process, of duration 1–3 h, by which free energy is accumulated in the magnetosphere and impulsively dissipated in the ionosphere [*Rostoker et al.*, 1980; *Rostoker*, 1999]. Although many aspects of substorm physics have been clarified over the preceding four decades, the triggering mechanism remains a subject of debate [e.g,. *Zhu et al.*, 2009; *Lyons et al.*, 2009]. Recent lines of investigation have focused on the flow of energy in the magnetosphere [*Angelopoulos et al.*, 2008]. From this perspective, the optical aurora must be treated as a proxy diagnostic. The primary response of the magnetosphere-ionosphere system to an impulsive change in magnetospheric configuration is in the convective flow, a fact convincingly demonstrated in the context of substorms by *Bristow and Jensen* [2007]. The aurora, while observationally accessible, is a secondary response, arising from the currents induced by these disturbances. The physical connection between convective disturbances and auroral morphologies defining the substorm phases remains poorly understood and inadequately observed. It is difficult to imagine a complete understanding of substorms that circumvents this physics.

[3] This work introduces a diagnostic strategy aimed at filling this gap. A technique is described for simultaneous imaging of convective flows and auroral forms. The enabling technology is the electronically steerable Poker Flat Incoherent Scatter Radar (PFISR) [see *Kelly and Heinselman*, 2009 and references therein]. Unlike dish antenna-based incoherent scatter radars (ISRs), PFISR can be configured to sample a three-dimensional ionospheric volume simultaneously. Such measurements can be used to construct volumetric images of ionospheric state parameters at a spatial resolution dictated by beam separation and temporal resolution dictated by available statistics [*Nicolls and Heinselman*, 2007; *Semeter et al.*, 2009]. Among the basic state parameters estimated in ISR analysis is bulk plasma velocity

[1]Department of Electrical and Computer Engineering and Center for Space Physics, Boston University, Boston, Massachusetts, USA.
[2]Physical Sciences Department, Embry-Riddle Aeronautical University, Daytona Beach, Florida, USA.
[3]SRI International, Menlo Park, California, USA.

0148-0227/10/2009JA014931

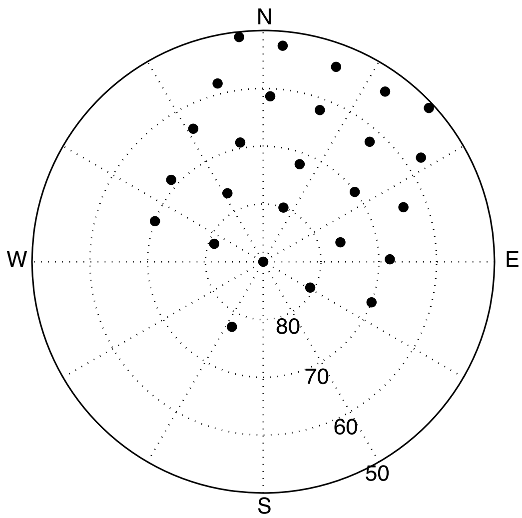

Figure 1. PFISR beam positions depicted on a radar-centered horizon coordinate system.

projected along the radar line of sight (LOS). When measured at multiple angles [*Doupnik et al.*, 1977; *Sulzer et al.*, 2005], or simultaneously from multiple ground locations [*Schlegel and Moorcroft*, 1989], the plasma velocity vector may be estimated via discrete inversion. In the present work, velocity measurements from a regular grid of beam positions are used to compute two-dimensional images of local convective flow. The flow fields are geographically registered with auroral images recorded by a collocated all-sky camera. The resulting composite image sequences provide a new perspective on the relationship between ionospheric flows and auroral forms.

[4] This technique is demonstrated using observations of a substorm with onset at ~1146 UT on 26 March 2008. The pulse pattern used in this experiment was not optimized for velocity field resolving; the time resolution of the computed flow fields was limited to 2 min (in future experiments, 30 s resolution is expected). Although this resolution precludes fully resolving substorm onset dynamics, interesting features are nonetheless observable. These include (1) localized attenuation of convective flow within arc elements, (2) attenuation to nearly zero of the aggregate flow field at substorm onset, (3) tangential flow at auroral boundaries irrespective of arc orientation with respect to the convection pattern, and (4) motion of auroral forms opposing the convective flow during substorm recovery. These observations are discussed in terms of current models of auroral electrodynamics.

2. Experiment Description

[5] PFISR is located at the Poker Flat Research Range (65.13°N, 147.47°W geographic) near Fairbanks, AK. The antenna is tilted toward the geomagnetic north so that its boresight direction corresponds to elevation 74° and azimuth 15°. For this experiment, PFISR was configured to cycle through a 5 × 5 grid of beam positions, plus an additional beam pointed in the magnetic zenith. The beam positions are depicted on a radar-centered horizon coordinate system in Figure 1.

[6] The pulse pattern used in this experiment consisted of an uncoded 480 μs pulse on one frequency channel (to probe the F region) and an alternating code [*Lehtinen and Häggström*, 1987] on the other channel (to probe the E region). Since the primary objective of this study is F region convective flow, only measurements by the uncoded pulse were used. This means we used only half of the available duty cycle. An increase in temporal resolution of at least a factor of 2 can be readily achieved in future experiments.

[7] Autocorrelation functions (ACFs) were formed from the gated returns at each beam position. The ACFs were then fitted using the standard four-parameter ISR model: N_e (electron density), T_e (electron temperature), T_i (ion temperature), and V_i (ion drift velocity). To obtain reasonable uncertainties in the fitting, the data were integrated for 2 min, corresponding to ~588 pulses per beam position. This level of analysis yields ionospheric state parameters at a discrete set of points (R, θ, ϕ). A further level of analysis, described in section 3, was then applied to produce two-dimensional images of convective flow and ion temperatures.

3. Method of Analysis

[8] Our method for estimating convective flow fields is a two-dimensional extension of *Heinselman and Nicolls* [2008, hereafter HN]. Above ~150 km altitude, the ion guiding-center drift is approximated by

$$\mathbf{v} = \frac{\mathbf{E} \times \hat{\mathbf{b}}}{B}, \tag{1}$$

where $\mathbf{E}$ is the electric field vector, $\hat{\mathbf{b}}$ is the unit magnetic field unit vector, and B is the magnetic field magnitude. As in the work by HN, we assume that parameters on the right-hand side of equation (1) are constant along a magnetic line of force from 150 km altitude through the maximum altitude probed by the radar (~400 km in this case). We assume that the geomagnetic reference frame defined by $\hat{\mathbf{b}}$ is approximated as a simple rotation of the geodetic reference frame according to the local magnetic inclination (dip angle) and declination. Figure 2 illustrates the observing geometry in two dimensions under these assumptions. Figure 2 lies in a magnetic meridional plane. Magnetic lines of force are depicted in orange. The blue arrows represent electric field vectors corresponding to $E \times B$ convective flow into the page. The abrupt change in E depicted is commonly observed at an auroral boundary [*Marklund*, 1984]. It is the development of such features from the quiescent convection pattern, and their relation to auroral activation, that we seek to resolve in this research.

[9] PFISR provides measurements of LOS velocity at a set of discrete points, depicted as black circles in Figure 2. Our objective is to invert groups of LOS measurements to produce an image of the overlying flow field. Although many approaches are possible, a simple pixelization (i.e., rectangular basis) was used in this work. The shaded area in Figure 2 illustrates one such velocity pixel. ISR analysis also provides scalar parameters T_e, T_i, and N_e which may be analyzed jointly with other diagnostic measurements. For instance, an image of T_i at 250 km, constructed via interpolation (Figure 2, right), provides a measure of the magnitude of the ion velocity by virtue of its connection with

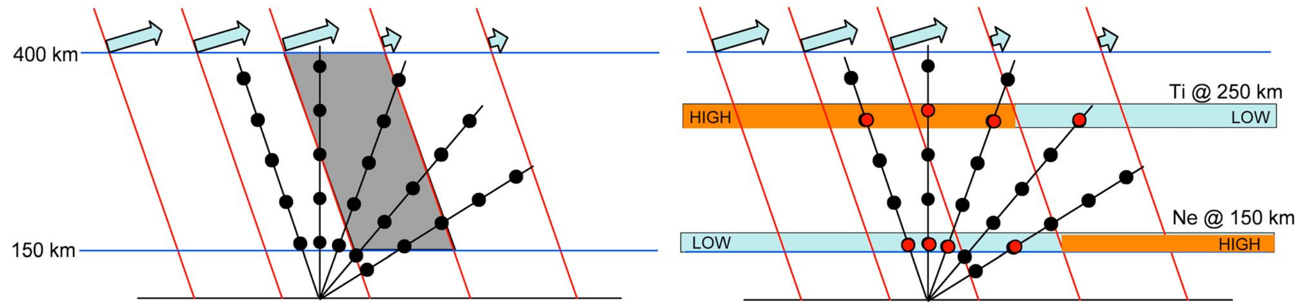

Figure 2. The technique for estimating convective flows used all measurements in a volumetric pixel (voxel) defined by (left) a magnetic flux tube coordinate system. These results can be compared with (right) other parameters extracted from a selected altitude.

frictional heating (see section 4.1). Similarly, N_e extracted at ~150 km altitude provides a measure of the location of auroral boundaries, owing to its connection with the auroral optical signal, although the horizontal region subtended at 150 km is quite limited compared with 250 km.

[10] There are two important assumptions in the aforementioned analysis strategy. First, the convection velocity is assumed to be uniform within each pixel. Violations in this assumption produce inconsistent data. However, the regularization approach applied here tends to suppress fluctuations arising from this. A second, more subtle caveat arises from the finite pulse length. The experiment used an uncoded 480 μs pulse, corresponding to 72 km of range. For oblique (to B) beam positions, some range gates may cut across an arc boundary, so there is a possibility of sheared flow within the range gate. This can produce distortions in the measured spectra which, in turn, can produce erroneous parameters in the fitting procedure [*Knudsen et al.*, 1993]. These caveats must be born in mind when interpreting such volumetric ISR measurements in nonuniform ionospheric regions.

[11] To develop a mathematical formulation of the flow field inversion, an unknown vector is first defined in the local geomagnetic coordinate system,

$$\mathbf{v} = \left[v_e \; v_n \; v_{\|}\right]^T, \tag{2}$$

where the subscripts e and n refer to field-perpendicular east and north directions, respectively, and $v_{\|}$ refers to the field-parallel component. Following HN, the LOS projection of this vector is given by

$$v_{\mathrm{LOS}} = \mathbf{k} \cdot \mathbf{v}, \tag{3}$$

where

$$\mathbf{k} = \begin{bmatrix} \cos\theta\sin\phi \\ \cos\theta\cos\phi \\ \sin\theta \end{bmatrix}^T \begin{bmatrix} \cos\delta & \sin I\sin\delta & -\cos I\sin\delta \\ -\sin\delta & \cos\delta\sin I & -\cos I\cos\delta \\ 0 & \cos I & \sin I \end{bmatrix}. \tag{4}$$

The projection matrix $\mathbf{k}$ has been broken into two parts. The right-hand term is a constant rotation matrix transforming the original velocity vector from geomagnetic to geodetic coordinates. This rotation is specified by the local magnetic inclination (dip) angle I and declination angle δ, taken as 77.5° and 22.5°, respectively. The other term describes the projection of the rotated vector along a line defined by elevation θ and azimuth ϕ in the radar-centered geodetic coordinates. The inverse problem consists of estimating the components of $\mathbf{v}$ in equation (2) from the observations. As described above, the observations were organized into spatial regions of interest, or "pixels," in the geomagnetic reference frame, resulting in a set of overdetermined inverse problems. The forward model for a given pixel observed by N projections, each with uncertainty e_{LOS} is written

$$\begin{bmatrix} v^1_{\mathrm{LOS}} \\ v^2_{\mathrm{LOS}} \\ \vdots \\ v^i_{\mathrm{LOS}} \\ \vdots \\ v^N_{\mathrm{LOS}} \end{bmatrix} = \begin{bmatrix} \mathbf{k}^1 \\ \mathbf{k}^2 \\ \vdots \\ \mathbf{k}^i \\ \vdots \\ \mathbf{k}^N \end{bmatrix} \mathbf{v} + \begin{bmatrix} e^1_{\mathrm{LOS}} \\ e^2_{\mathrm{LOS}} \\ \vdots \\ e^i_{\mathrm{LOS}} \\ \vdots \\ e^N_{\mathrm{LOS}}, \end{bmatrix}, \tag{5}$$

where $\mathbf{k}^i = \mathbf{k}(\theta^i, \phi^i)$ is the projection vector (direction cosine) corresponding to v^i_{LOS}. Equation (5) may be cast as a matrix equation

$$\mathbf{v}_{\mathrm{LOS}} = A\mathbf{v} + \mathbf{e}_{\mathrm{LOS}}, \tag{6}$$

where A (dimensions $N \times 3$) is the forward model for which a pseudoinverse is sought.

[12] Velocity vectors were estimated in the geomagnetic reference frame and then projected back into cartesian coordinates for comparison with optical measurements via the transformation

$$[x \; y \; z] = R\mathbf{k}(\theta, \phi), \tag{7}$$

where R is range to the center of a velocity pixel. Figure 3 shows a projection of the measurement positions in the $z = 0$ plane for our experiment. The plot includes only samples from altitudes between 150 and 400 km, where equation (1) holds. The samples were organized into a 4 × 4 grid of pixels, with pixel centers covering a region of approximately 100 × 100 km. The pixels were configured to overlap by 50% neighboring pixels in each orthogonal direction. Two such pixels are identified by blue and red squares. This overlap enforces correlation between neighboring pixels and is equivalent to enforcing a spatial smoothness constraint.

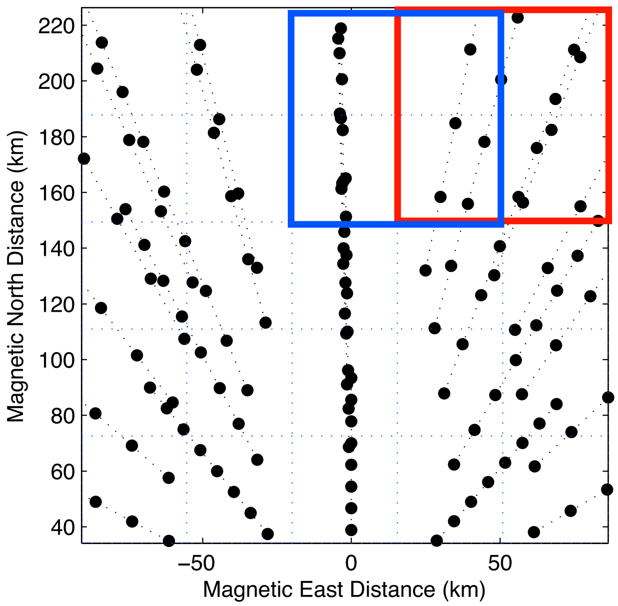

Figure 3. Projection of LOS velocity samples (circles) into the $z = 0$ plane using equation (7). Examples of two of the overlapping square pixels used in the inversion are shown in red and blue.

[13] The pixelization was chosen to meet the constraint that each pixel be intersected by four beams. In the case of noiseless measurements, multiple measurements along a given beam (corresponding to a given **k**) provide no additional information over a single measurement (assuming uniform flow within the pixel). However, in the presence of noise, multiple measurements serve to reduce statistical uncertainties, which is an important consideration for the inherently ill-conditioned nature of the inversion.

[14] Equation (6) was solved for each pixel using the Bayesian estimator introduced by HN,

$$\hat{\mathbf{v}} = \Sigma_v A^T \left(A \Sigma_v A^T + \Sigma_e \right)^{-1} \mathbf{v}_{\mathrm{LOS}}, \tag{8}$$

where Σ_e is a diagonal error covariance matrix, with elements equal to the variances estimated in the ISR fitting procedure, and Σ_v is a prescribed prior covariance model for **v**. For this work, the variance for $\hat{b}_\perp$ components of **v** was set to $(3000\ \mathrm{m/s})^2$, as in the work by HN. This value suppresses extreme outliers, while allowing for the full expected range of variability in v. The $B_\|$ component of **v** is generally small compared to the $B_\perp$ component over the range of altitude range considered here (150–400 km). Even within regions of strong topside ion upwelling, $v_\|$ is a few tens of meters per second below 400 km altitude [*Wahlund et al.*, 1992; *Semeter et al.*, 2003; *Zettergren et al.*, 2007], while convective flows are typically in the range of 1–4 km/s at high latitudes [*Whalen et al.*, 1974]. We enforce this physical difference between the magnitudes of perpendicular and parallel flow components in order to constrain the null-space of the inversion. Specifically, we set $\Sigma_{v\|}$ to $(15\ \mathrm{m/s})^2$ in our calculation to force the estimator to favor solutions with small $B_\|$ flow.

[15] The uncertainty in the computed flow field can be evaluated quantitatively by propagating the error estimate in the LOS velocities through equation (8). These uncertainties are plotted in Figure 4 as ellipses for a particular flow field example (Figure 14d). The ellipses correspond to one standard deviation, i.e., 39.4% probability that the velocity vector lies on or within the ellipse. The uncertainties are generally in the range of 10%–20% of the estimated values and become worse downrange from the radar, owing to less independent information between adjacent k vectors.

4. Results

[16] The experiment described in section 2 was run during a 24 h geomagnetically active period on 26 March 2008. The presentation of results is organized as follows. We first provide a rough validation of the velocity inversion procedure via comparison with ion temperature measurements. Next, we examine the aggregate behavior of the flow fields and auroral forms during the three canonical substorm phases: growth, expansion, and recovery. Finally, we describe two events where local nonuniformities (shears) in flow are correlated with specific boundaries in the auroral images. The first shows the energization of an arc element within a quiet east-west arc during the growth phase; the second shows the behavior of flows along a translating north-south boundary in the recovery phase. The results suggest some specific new insights into substorm magnetosphere-ionosphere coupling.

4.1. Validation of Flow Fields Using T_i

[17] In the work by HN, results were validated via direct comparison with measurements from a rocket overflight. In lieu of an independent velocity diagnostic either from rocket or conjugate satellite, we may use estimates of T_i, also provided in the ISR fitting. Specifically, in the altitude range of about 140–300 km, the dominant terms in the ion energy equation are frictional heating and collisional cooling, leading to an explicit relationship between T_i and $v = |\mathbf{v}|$ [*St.-Maurice et al.*, 1999]:

$$T_i = \frac{v^2 M_n}{3k} \left[\left(\frac{\nu_{\mathrm{in}}}{\Omega_i} \right)^2 + 1 \right]^{-1} + T_n, \tag{9}$$

where M_n is average neutral mass, k is Boltzman's constant, ν_{in} is ion-neutral collision frequency, Ω_i is the ion gyro frequency, and T_n is neutral temperature. In ISR analysis, T_i is primarily a measure of the width of the ISR spectrum, while v is derived from the bulk Doppler shift of the spectrum. These parameters are nearly independent in the ISR fitting procedure. Thus, we may use equation (9) to provide some measure of confidence in our estimates of **v**.

[18] Figure 5 gives three examples of computed ion velocity vectors (arrows) overlaid on a contour plot of ion temperature (contours). The velocity vectors were computed using all LOS measurements above 150 km, as discussed in section 3; ion temperatures were extracted at an altitude of 240 km through interpolation of parameters derived from the fitted spectra. These examples were chosen because the relative uniformity of the flows and temperatures within the field. The results illustrate the expected positive correlation between ion velocity and ion temperature predicted by equation (9). The comparison is better quantified in Figure 6, which shows a scatterplot of v versus T_i for the 1130–

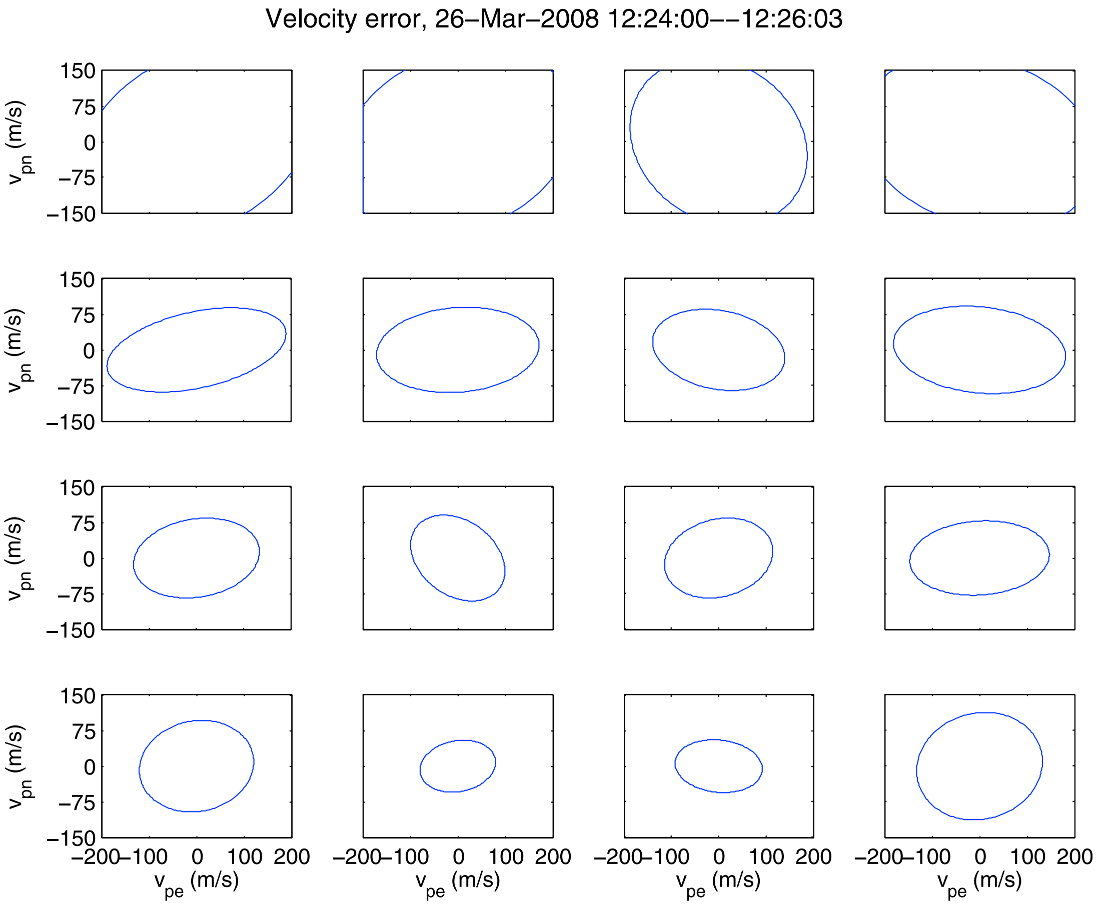

Figure 4. Error ellipse corresponding to the flow field shown in Figure 14d.

1230 UT interval. Although the spread is significant, the parabolic relationship between v and T_i, predicted by equation (9), can be readily identified in the data. The solid line in Figure 6 shows the theoretical result computed using equation (9), with neutral parameters computed using the NRL-MSIS-00 empirical model [*Picone et al.*, 2002]. The model result is seen to provide a reasonable fit to the observed trend.

4.2. Composite Imaging: Selected Intervals

[19] To investigate the relationship between auroral forms and two-dimensional flow fields, we focus on an isolated substorm with onset near 1146 UT. Figure 7 shows the

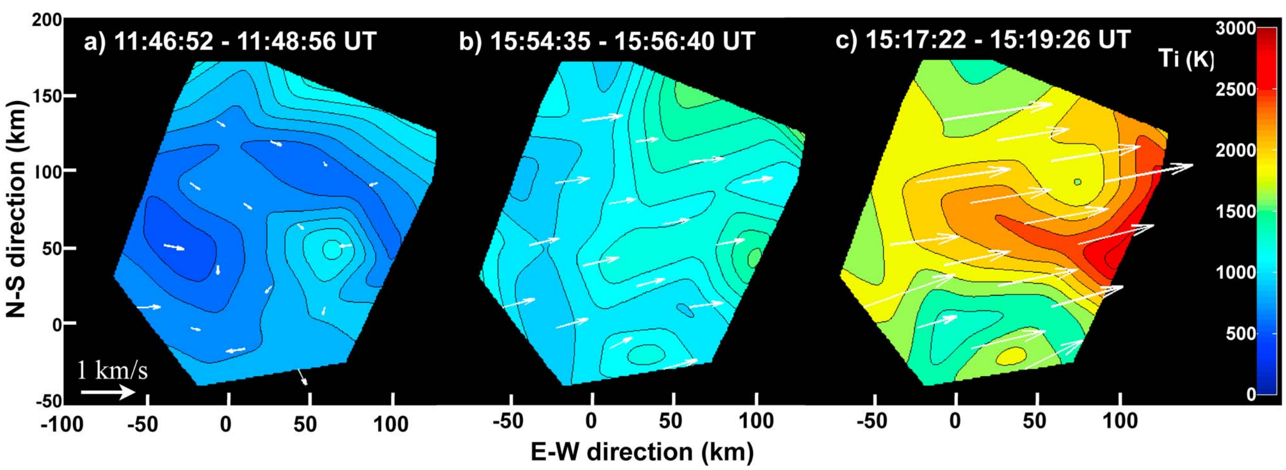

Figure 5. Examples of **v** and T_i (at 240 km altitude) derived from PFISR analysis. T_i is well correlated with $|\mathbf{v}|$, as predicted theoretically.

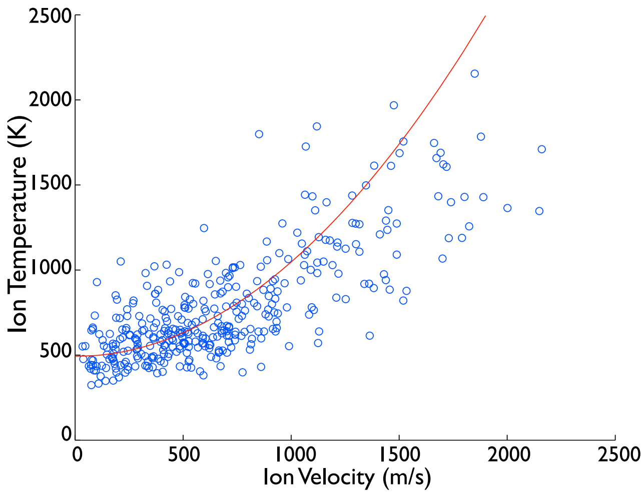

Figure 6. Scatterplot of |**v**| versus T_i for a 1 h period encompassing the substorm onset at 1146 UT.

H, *D*, and *Z* components measured by the Poker Flat magnetometer. This substorm was characterized by a particularly rapid onset, as illustrated in the steplike development of a negative bay in the *H* component.

[20] Figure 8 gives another view of this substorm. Shown are the brightness versus elevation and time for four prominent optical emission lines, as measured by the Poker Flat meridional scanning photometer (MSP). Electron aurora is indicated in the oxygen 557.7 nm and N_2^+ 427.8 nm channels; proton aurora is indicated in the H_β 486.1 nm channel. The growth phase is characterized by the initiation of southward propagating auroral forms in all channels near 1100 UT. An explosive onset occurs near 1146 UT, saturating the 427.8 nm channel. The horizontal lines demarcate the angular field of view (FOV) of PFISR in the meridional direction. The onset arc was equatorward of the PFISR FOV, but the brightest auroral forms during the expansion phase were within the PFISR FOV near 40° elevation as indicated in the 557.7 nm channel.

[21] Before comparing individual flow fields and images, it is instructive to examine the aggregate behavior of plasma flows and optical brightness over the substorm period. The blue curve in Figure 9 shows 557.7 nm brightness extracted from the MSP measurements (Figure 8) at 42° elevation (near the poleward edge of the PFISR FOV). The green curve plots magnitude of the horizontal flow velocity in this region, as estimated from PFISR measurements. The convective flows in this region are seen to increase in an approximately monotonic fashion from 1100 to 1135 UT. At this point, this region is traversed by a southward propagating growth-phase arc. Flows are greatly attenuated within the arc and increase again once the arc passes. The substorm onset at 1146 UT is accompanied by another large reduction in flow speed. The usual interpretation of this anticorrelation holds that the reduction in flow corresponds to a reduction in electric field, which is required to maintain current continuity in the presence of a local enhancement in ionospheric conductance [*Marklund*, 1984]. However it also is clear that the flow and luminosity are not strictly antic-

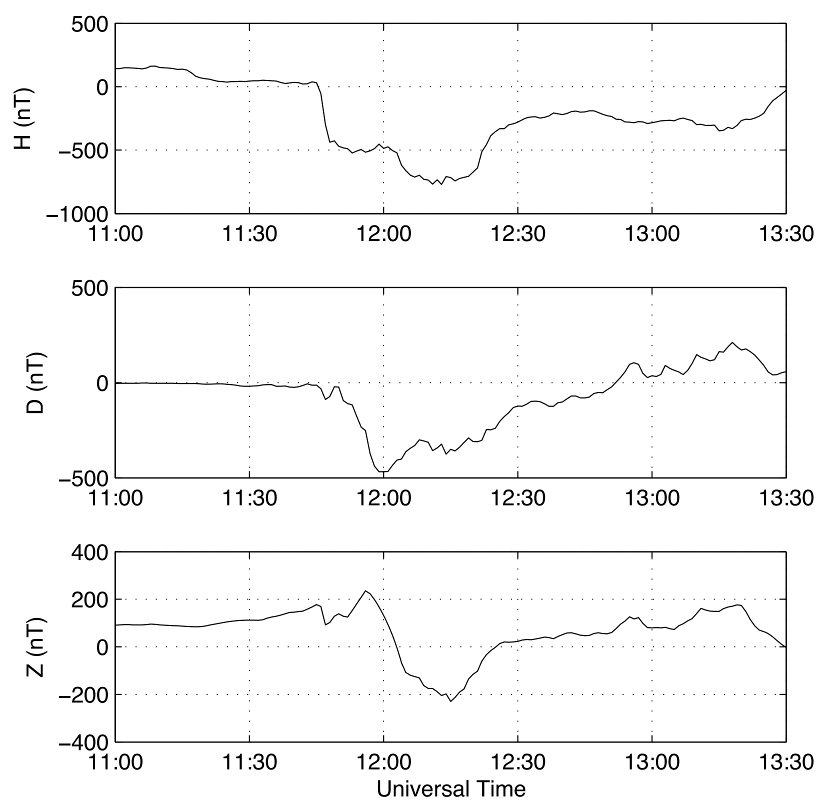

Figure 7. Poker Flat magnetometer trace (orthogonal *H*, *D*, and *Z* components) on 26 March 2008 highlighting a substorm onset near 1146 UT.

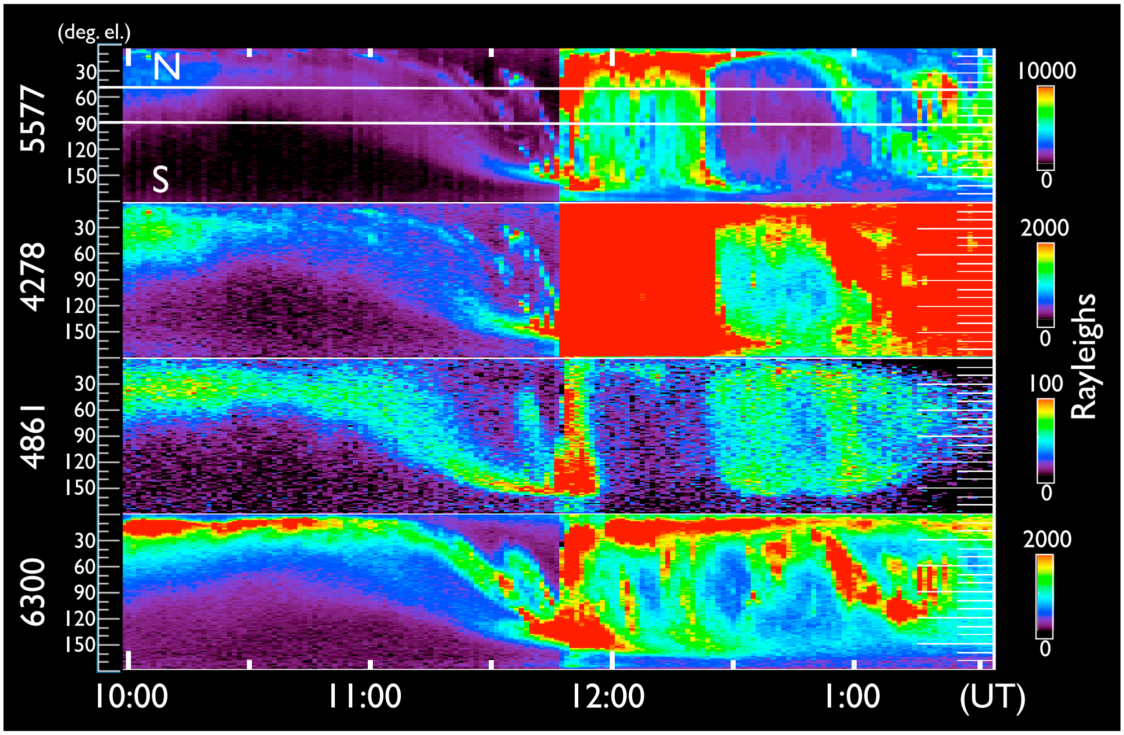

Figure 8. Observations by the Poker Flat meridional scanning photometer (MSP) on 26 March 2008. Figure 8 shows brightness versus time and elevation angle for four prominent auroral emission features. The 427.8 nm and 557.7 nm channels indicate electron aurora, the 486.1 nm channel indicates proton aurora, and the 630 nm channel is due to a combination of ionization and excitation photochemistry. The present study focuses on the onset near 1146 UT.

orrelated during this period. Indeed, during the recovery phase the flow speed recovers to the large preonset levels of ~800 m/s even in the presence of continued auroral production. The flow speed is maintained at these enhanced values even after the passage of the optical forms through the field near 1225 UT.

[22] We now turn to a closer examination of the spatiotemporal relationship between the auroral forms and ionospheric flows. Three examples are presented. In the first example, we examine the aggregate behavior of flows during the three canonical substorm phases, growth, expansion, and recovery, confirming the observation of established morphologies. For this work, the identification of substorm phases rests primarily on the relative behavior of convective flows and auroral forms. The second example concerns composite images of ion flows, ion temperatures, and auroral morphology during a period characterized by a local activation of an auroral arc element during the growth phase. The third example considers the westward movement of a dynamic auroral boundary.

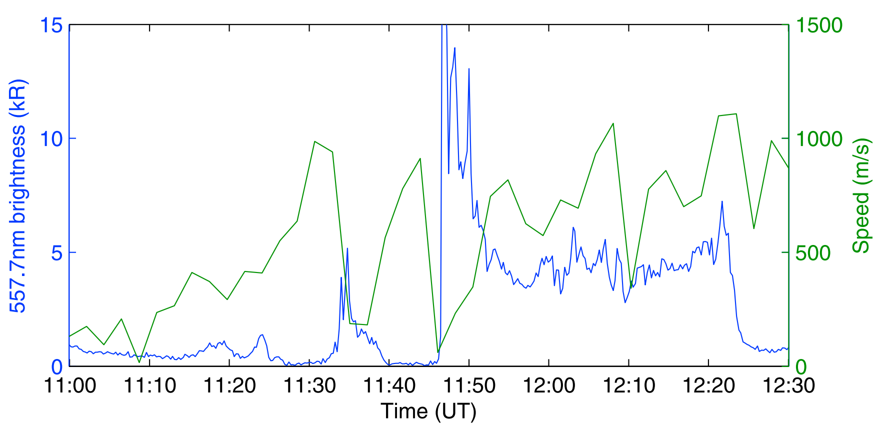

Figure 9. Blue shows 557.7 nm brightness extracted at 42° elevation from the MSP observations in Figure 8 encompassing the time period of the substorm. Green shows *F* region ion flow speed in the same region.

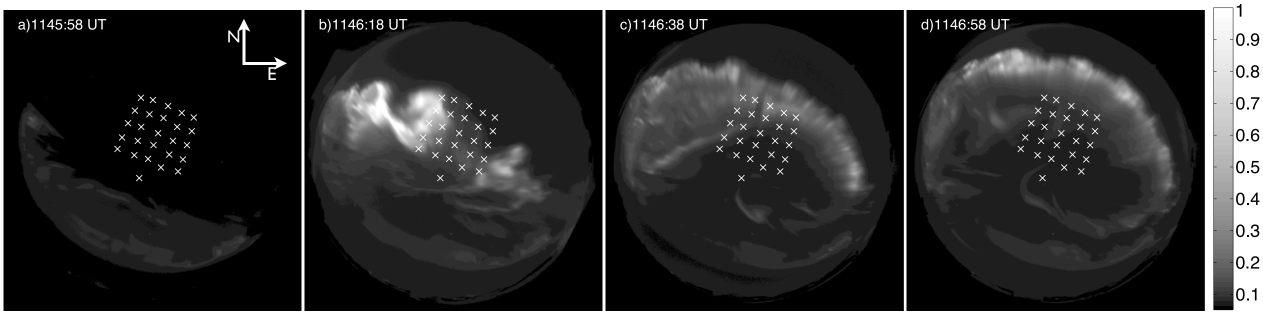

Figure 10. All-sky images recorded around the time of expansion phase onset.

4.2.1. Example 1: Aggregate Flows During Canonical Substorm Phases

[23] Figure 10 shows all-sky images of the onset recorded by a collocated white-light camera operating at 20 s cadence and 0.5 s exposure. The PFISR beam positions in angular coordinates are indicated by "x"s. (Note that the images have been flipped left to right to maintain consistency with the horizon coordinate system used in Figure 1, i.e., north is toward the top and east is toward the right.) The onset occurred in the 20 s interval between Figures 10a and 10b. A quasi-logarithmic grayscale map has been applied (linear scale has raised to the power of 0.6) in order to resolve the factor of 10 variation in luminosity between the preonset auroras to the south in Figure 10a and the breakup arcs in Figures 10b and 10c. A movie version of complete all-sky observations recorded over this period can be found at http://heaviside.bu.edu/shared/Allsky_26Mar2008.avi.

[24] Figure 11 shows coregistered ion flow fields and auroral forms during the growth phase (top), expansion phase (middle), and the early recovery phase (bottom) of the substorm. Auroral images have been geographically registered assuming an emission altitude of 120 km. The axes give ground distance referenced to geographic north and east. The PFISR array and, hence, flow fields are oriented toward magnetic north. The flow field in each row corresponds to a particular 2 min radar integration window, indicated in the left frame of each row. The columns show three sample auroral images recorded within the radar integration window. The auroral images in each row have been individually scaled to account for the large variability in auroral brightness among the substorm phases.

[25] Figure 11 (top) shows the magnetic southward propagation of an east-west growth phase arc within the convection pattern. The arc propagates southward at a uniform velocity of ~500 m/s. The ion flow is approximately uniform in magnitude across the field (~1 km/s). The direction of flow is generally toward the magnetic southeast. The observations were made in the postmidnight auroral zone, where an eastward return flow is expected. The southward component of the flow is roughly equal to the observed southward velocity of the arc, suggesting that the arc is entrained in the convective flow at this time. The observations show the expected ionospheric manifestation of plasma sheet stretching prior to substorm onset [*McPherron*, 1972].

[26] Figure 11 (middle) summarizes flows and auroral forms encompassing the expansion phase onset. Compared with Figure 11 (top), the flows are greatly reduced in this period. The rapid attenuation of ion flow at onset has been well established [*Bristow et al.*, 2003]. As discussed in the beginning of section 4.2, the usual explanation invokes current continuity in a region of rapidly increasing conductivity; specifically, assuming a constant horizontal current, an increase in conductance caused by auroral ionization must be accompanied by a decrease in E in order to maintain current continuity.

[27] Figure 11 (bottom) is representative of the early recovery phase. The eastward component of the flow is similar in magnitude to the preonset flow pattern, but the southward component is greatly reduced. This is further confirmation that the southward flows in the top row were associated with growth phase dynamics.

4.2.2. Example 2: Activation of an Arc Element During the Growth Phase

[28] The previous example focused on the average behavior of vectors in each flow field. Such an analysis did not require the full 26 beams used in the experiment; a single average flow vector could have been estimated using just a few beams. Sections 4.2.2 and 4.2.3 treat more interesting examples where spatial variations in the flow field can be identified and compared with auroral morphologies.

[29] Figure 12 shows a sequence of all-sky images ~12 min prior to onset documenting the activation of an arc element (upper right of each frame). The period of activation lasted for over a minute, so it is reasonable to investigate comparisons with flow patterns derived from 2 min radar integrations. Figure 13 shows coregistered flow fields (arrows), ion temperatures (colored contours), and auroral images during three contiguous 2 min integration windows: before, during, and after the arc element activation. The flow fields are overlain on representative optical images recorded during each window. Figure 13a shows a region of high ion temperatures and large tangential flows between the two "quiet" arcs. When the arc element is illuminated (Figure 13b), the flow in this region is reduced, and the T_i field shows a distinct reduction in this region. Together, these features indicate a local attenuation of the electric field within the arc element.

[30] Interestingly, Figure 13a shows that the flows and temperatures are particularly large in this region prior to the formation of the auroral element. Although the temporal resolution is too poor to state definitively, the observations provide evidence for a possible precursor to the auroral activation in the convective flow. In Figure 13c, this region of reduced flow velocities spreads westward and equator-

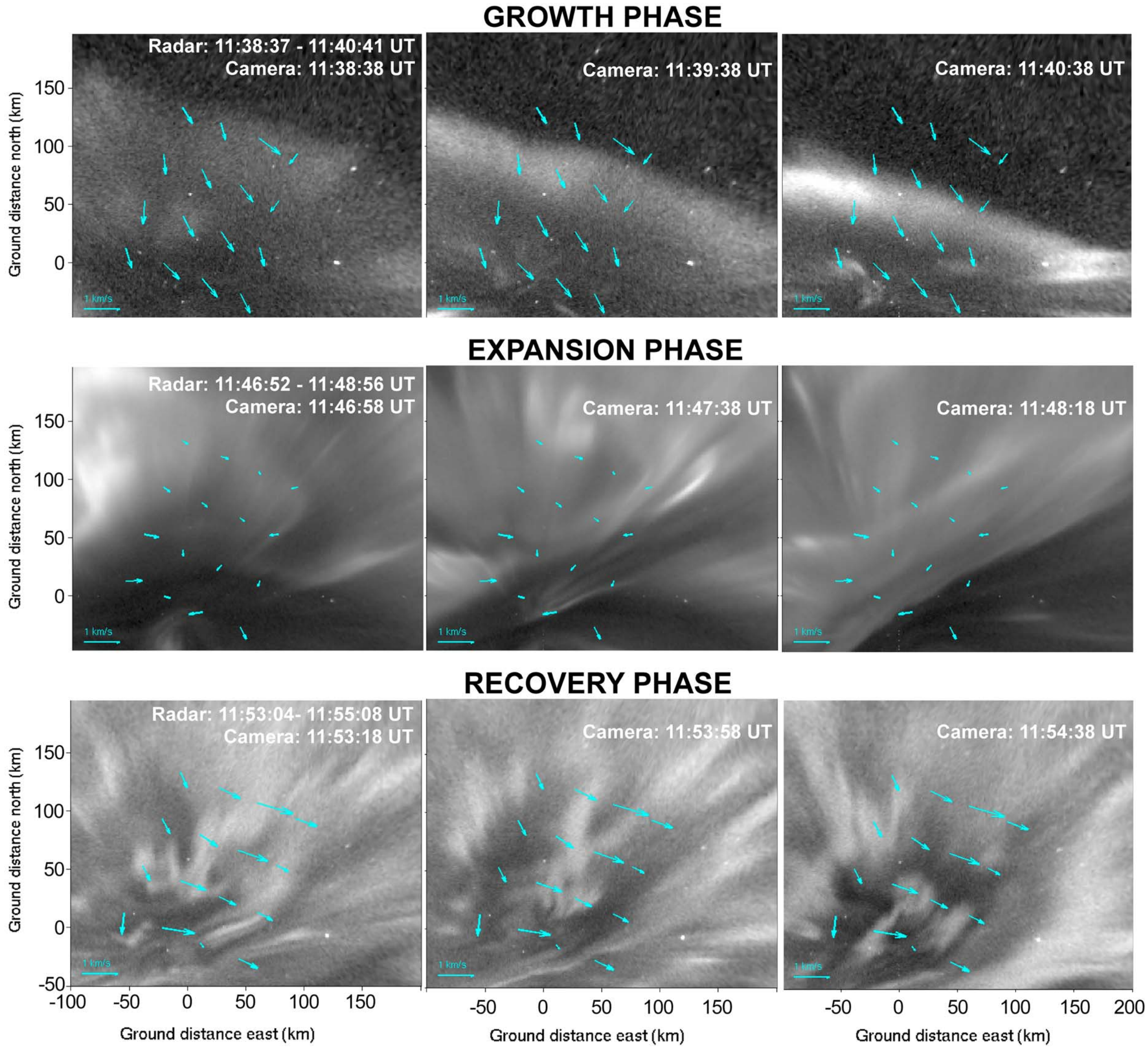

Figure 11. Coregistered ion flow fields and auroral forms sampled during the canonical substorm phases: (top) growth phase, (middle) expansion phase, and (bottom) early recovery phase. Each row corresponds to a single PFISR integration window; the columns show representative auroral images recorded during these windows.

ward as the activated element dissipates. Flows in the equatorward part of the image have increased, as the arc in this region has propagated equatorward, nearly out of the PFISR field of view. This temporal morphology is consistent with the term "pseudobreakup," as described by *Lyons et al.* [2002], although the poleward location of this event is more consistent with a "poleward boundary intensification" [*Lyons et al.*, 2000].

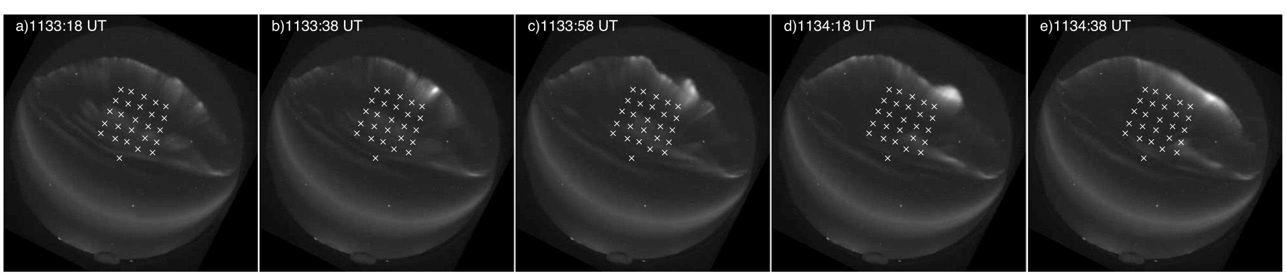

Figure 12. All-sky images recorded ~12 min prior to substorm onset. The sequence documents the activation of an arc element in the upper right of each frame.

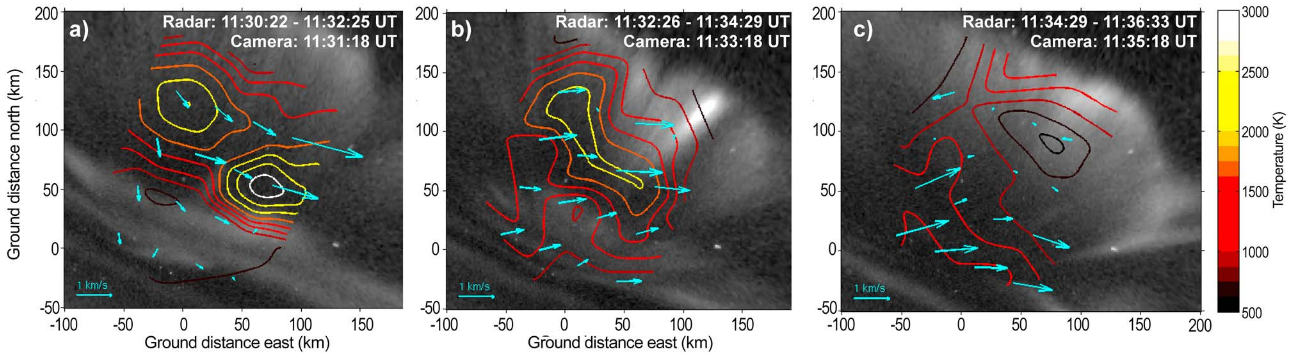

Figure 13. Composite presentation of flows (arrows), ion temperatures (contours), and auroral forms during the arc element activation of Figure 12.

4.2.3. Example 3: Auroral Boundary Dynamics During Recovery Phase

[31] Figure 14 documents the westward passage of a dynamic north-south auroral boundary through the field of view during the late expansion/early recovery phase. The time labels indicate the starting time for both the radar and optical diagnostics. However, as in Figure 11, the radar cadence is 2 min, while the optical cadence is 20 sec. There are several noteworthy observations in these images. Consider first the flow field. Inside the luminous region (e.g., vectors in Figure 14a) and outside the luminous region (vectors in Figure 14f), the flows are similar in magnitude and direction, directed eastward. This result is in contrast with the results of Figures 11 and 13, where flows within the aurora were attenuated.

[32] The flows near the boundary in Figure 14 are rotated into the tangential (southward) direction, consistent with a localized electric field directed into the auroral region. This morphology is consistent with the morphology observed in Figure 13, albeit the entire system has been rotated 90° in the recovery phase.

[33] Consider next the motion of the optical forms. The boundary, on average, moved westward in this image sequence, but the convective flow is consistently eastward (except at the boundary). This suggests that the aurora has a large apparent motion relative to the plasma reference frame, a feature termed "proper motion" by *Haerendel et al.* [1993]. However, the boundary does not have a simple dynamic. Examining individual 20 s frames in this sequence, there is evidence for transient production of new auroral forms along this boundary. Although the aurora is not fully resolved at this cadence, these newly developed features do not appear to move with the auroral boundary. A similar dynamic has been reported by *Semeter et al.* [2008] using higher-resolution equipment and interpreted as a dif-

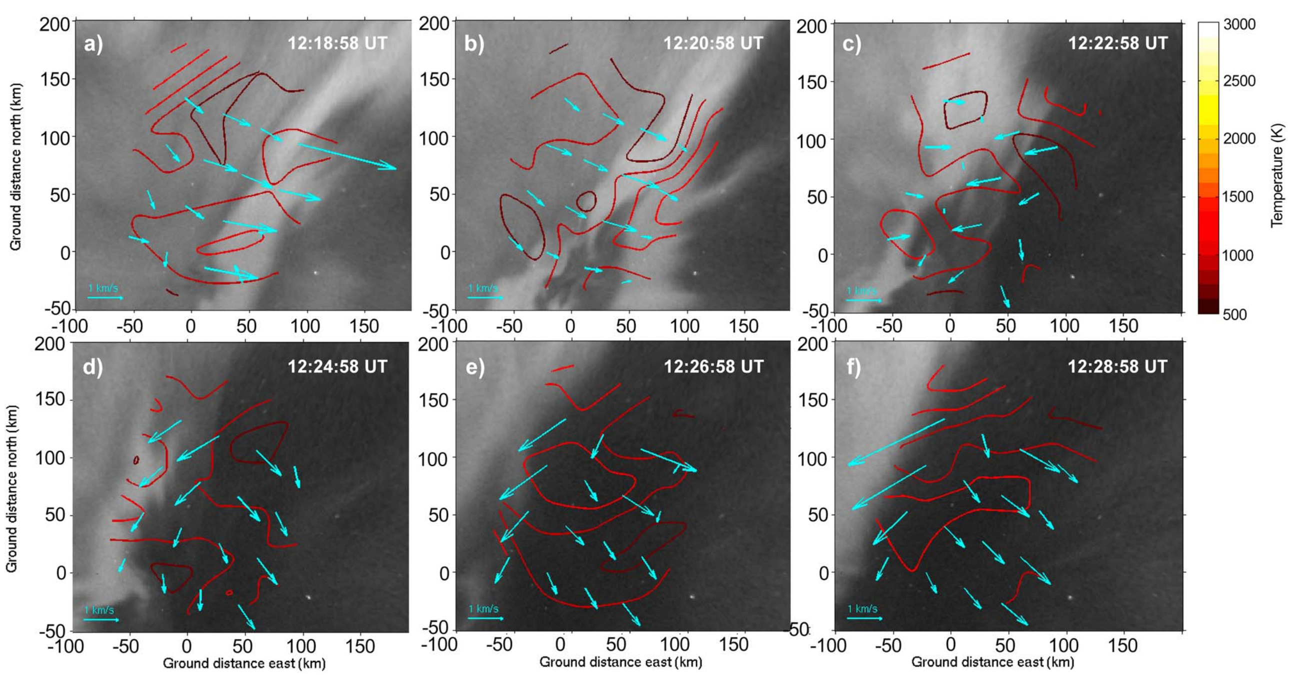

Figure 14. Flow fields associated with a dynamic auroral boundary during the substorm recovery phase.

ferential phase and group motion associated with a dispersive Alfvén wave.

[34] Finally, note that the ion temperature (color contours) is not well correlated with flow velocity, as it was in Figure 13. Some speculations about the cause of this discrepancy between growth- and recovery-phase dynamics are discussed in section 5.

5. Discussion and Summary

[35] A composite imaging technique has been introduced with the goal of clarifying the time-dependent relationship between disturbances in ionospheric convection and changes in auroral morphology. Related efforts by the HF radar community have focused on establishing large-scale patterns in convective flows and auroral forms during the substorm cycle [e.g., *Bristow et al.*, 2003; *Grocott et al.*, 2009; *Zou et al.*, 2009]. By contrast, this work seeks to clarify the time-dependent connections between localized variations in the convective flow and auroral arc dynamics.

[36] The enabling technology for this effort is PFISR, the first electronically steerable phased-array incoherent scatter radar. PFISR can be configured to cycle through a regular grid of beam positions on a pulse-by-pulse basis, accumulating statistics simultaneously from all sampled directions, analogous to the way data are acquired in a digital camera. However, unlike a camera, PFISR also resolves range, enabling the construction of volumetric images of plasma state parameters. This capability has been exploited already in the study of a variety of ionospheric phenomena [*Nicolls and Heinselman*, 2007; *Nicolls et al.*, 2007; *Semeter et al.*, 2009].

[37] The present study constitutes the first attempt to exploit this volumetric sampling capability to form two-dimensional images of ionospheric convective flow. The analytical technique applied is a two-dimensional extension of the technique described by HN. Their work applied the standard assumption used in most prior studies of auroral zone convection using ISR, namely, that the flows are ordered by magnetic latitude. For large-scale, or average, behavior, this configuration is sensible. However, during active auroral conditions, field geometries and auroral morphologies can become complex, and the most meaningful coordinates for interpreting flows become the auroral boundaries themselves. In the present study, examples of flows oriented in both the east-west (Figure 13) and north-south (Figure 14) direction were found. In each case, the flow fields were unambiguously correlated with auroral boundaries.

[38] The resolution achievable in this work was 30 km spatial and 2 min temporal over a 100 × 100 km field of view. This resolution is clearly insufficient to fully resolving the dynamic time scales of substorm onset. The temporal resolution can be improved by a factor of at least 2 using a more optimal pulse pattern. Another factor of 2 may soon be possible owing to an anticipated increase in the PFISR transmit power. This suggests that <30 s temporal resolution will be possible. This time scale is shorter than the travel time to any putative generator region. As such, the technique becomes relevant to evaluating Alfvén resonance and feedback models for auroral formation [e.g., *Atkinson*, 1970; *Sato*, 1978; *Lysak and Song*, 2002] and substorm onset [*Cheng et al.*, 2009]. The limitations in spatial resolution, on the other hand, are inherent in the monostatic viewing geometry. Better spatial resolution requires closer beams. But, as the beams become closer, the measurements become more correlated, precluding reliable estimation of the vector velocity. Thus, there is an inherent tradeoff between spatial resolution and reliability of the results using a monostatic radar.

[39] Even with the resolution of the current experiment, conclusive and interesting results were obtained via careful analysis of coregistered radar and optical results. The first example confirmed well-known large-scale morphologies of the convection pattern during the substorm cycle, namely, a southward component of the convective flow during the growth phase, the suppression of the convection electric field within the auroral breakup region, and the recovery of convective flows to their quiescent levels during the recovery phase. In examples 2 and 3, spatial structure in the flow field was observed that was well correlated with auroral dynamics. Example 2 documented the local attenuation of the electric field in the region of a pseudobreakup initiation [*Lyons et al.*, 2002]. Figure 13b showed a clear spatial anticorrelation between auroral luminosity (hence, conductivity) and velocity (hence, electric field). The region of elevated T_i, in fact, was seen to track around the activated arc element. Examining the flow field in the previous integration period (Figure 13a) revealed intriguing evidence of a local enhancement in flow and temperature near the region where the arc activation occurred. An enhancement in convection prior to onset of a full substorm is a well-documented feature [*Bristow and Jensen*, 2007]. This observation of similar behavior supports the assertion by *Lyons et al.* [2002] that pseudobreakups follow the same basic cycle. Higher-resolution measurements will greatly clarify this dynamic, including possible oscillatory behavior connected to Alfvén wave dynamics.

[40] Example 3 (Figure 14) documented the westward motion of a north-south auroral boundary within a region of quiescent eastward flow during the recovery phase. This example revealed several features that contrasted with example 1. First, the variations in flow velocity near the boundary were not accompanied by attendant variations in T_i, as they were in Figure 13. This could indicate the presence of a substantial neutral wind aligned with the plasma flows, which reduces frictional heating [*Thayer*, 1998]. It may also indicate a violation of our analysis assumptions; for example, our assumption that the field-parallel component of $\mathbf{v}$ is small. This could also simply be a manifestation of undersampling in space and time a highly dynamic plasma boundary. Higher-resolution measurements by both the radar and camera will greatly clarify these issues.

[41] A second contrasting observation was the large relative motion between the auroral forms and the background plasma convection. This large "proper motion" [*Haerendel et al.*, 1993] of the aurora is suggestive of an electrical decoupling between the magnetosphere and ionosphere in this interval. However, the optical measurements suggest that a more nuanced interpretation may be called for. The boundary appears to be characterized by a periodic formation of transient arcs which do not follow the average motion of the boundary. This dynamic was observed by *Semeter et al.* [2008] and interpreted with respect to phase and group motion within an Alfvén resonant cone. Again,

higher-resolution measurements will clarify the various apparent motions observed at this boundary.

[42] Third, there was no attenuation of flows within the illuminated region, as observed in Example 1. The only variation observed was the rotation of the velocity vectors at the auroral boundary toward a direction consistent with a localized electric field pointing into the arc. It is worthwhile to examine these discrepancies between Figures 13 (growth phase) and 14 (recovery phase) in the context of prior attempts to classify auroral electric field patterns. Specifically, *Marklund* [1984] identified two physically based morphologies, termed "polarization" arcs and "Birkeland" arcs. A polarization arc is characterized by an anticorrelation between electric field and conductivity, which develops as a requirement to maintain continuity in horizontal current across a gradient in conductance. Such a scenario is consistent with Figures 11 and 13. The recovery phase scenario (Figure 14), on the other hand, exhibits a morphology more consistent with a Birkeland arc, where current continuity is maintained via field-aligned currents. The flows in Figure 14 are similar in magnitude and direction inside and outside the arc; that is, there is no apparent correlation of electric field with conductivity. The only variation in flow occurs at the auroral boundary. This scenario is consistent with a boundary that demarcates an up-down Birkeland current pair.

[43] Time dependence was not addressed by *Marklund* [1984], except to mention that aspects of both arc types could be present simultaneously in a dynamic situation. Of particular importance is the role of Alfvén waves, which are the mechanism by which changes in free energy are communicated between the magnetosphere and ionosphere. Indeed, in a purely MHD picture, a substorm disturbance would undergo multiple reflections in this system until a new equilibrium is reached [*Tanaka*, 2007]. Although the aurora is a convenient diagnostic of magnetospheric dynamics, the formation of the aurora acceleration region is a secondary effect, lying in the realm of plasma kinetic theory. The coupling of the ideal MHD description to the nonlinear wave-particle coupling that leads to the aurora has not been clearly established, either observationally or theoretically [*Haerendel*, 2007]. The results shown here highlight the fact that there is no simple static description relating ionospheric electric fields and auroral forms.

[44] **Acknowledgments.** The authors would like to acknowledge Don Hampton for assisting with the camera data used in this work and Larry Lyons for valuable discussions about data interpretation. The PFISR facility was developed under a grant from the National Science Foundation. Additional support for this work was provided by NSF grants AGS-0946304 and AGS-0946611.

[45] Zuyin Pu thanks Shasha Zou and William Bristow for their assistance in evaluating this paper.

References

Akasofu, S.-I. (1964), The development of the auroral substorm, *Planet. Space Sci.*, *12*, 273–282, doi:10.1016/0032-0633(64)90151-5.

Angelopoulos, V., et al. (2008), First results from the THEMIS mission, *Space Sci. Rev.*, *141*, 453–476, doi:10.1007/s11214-008-9378-4.

Atkinson, G. (1970), Auroral arcs: Result of the interaction of a dynamic magnetosphere with the ionosphere, *J. Geophys. Res.*, *75*, 4746–4754, doi:10.1029/JA075i025p04746.

Bristow, W. A., and P. Jensen (2007), A superposed epoch study of SuperDARN convection observations during substorms, *J. Geophys. Res.*, *112*, A06232, doi:10.1029/2006JA012049.

Bristow, W. A., G. J. Sofko, H. C. Stenbaek-Nielsen, S. Wei, D. Lummerzheim, and A. Otto (2003), Detailed analysis of substorm observations using SuperDARN, UVI, ground-based magnetometers, and all-sky imagers, *J. Geophys. Res.*, *108*(A3), 1124, doi:10.1029/2002JA009242.

Cheng, C.-C., C. T. Russell, V. Angelopoulos, I. Mann, K. H. Glassmeier, U. Auster, and W. Baumjohann (2009), THEMIS observations of consecutive bursts of Pi2 pulsations: The 20 April 2007 event, *J. Geophys. Res.*, *114*, A00C19, doi:10.1029/2008JA013538, [printed 115(A1), 2010].

Doupnik, J. R., A. Brekke, and P. M. Banks (1977), Incoherent scatter radar observations during three sudden commencements an a Pc 5 event on August 4, 1972, *J. Geophys. Res.*, *82*, 499–514, doi:10.1029/JA082i004p00499.

Grocott, A., J. A. Wild, S. E. Milan, and T. K. Yeoman (2009), Superposed epoch analysis of the ionospheric convection evolution during substorms: Onset latitude dependence, *Ann. Geophys.*, *27*, 591–600.

Haerendel, G. (2007), Auroral arcs as sites of magnetic stress release, *J. Geophys. Res.*, *112*, A09214, doi:10.1029/2007JA012378.

Haerendel, G., S. Buchert, C. La Hoz, B. Raaf, and E. Rieger (1993), On the proper motion of auroral arcs, *J. Geophys. Res.*, *98*, 6087–6099, doi:10.1029/92JA02701.

Heinselman, C. J., and M. J. Nicolls (2008), A Bayesian approach to electric field and *E*-region neutral wind estimation with the Poker Flat Advanced Modular Incoherent Scatter Radar, *Radio Sci.*, *43*, RS5013, doi:10.1029/2007RS003805.

Kelly, J. D., and C. J. Heinselman (2009), Initial results from Poker Flat Incoherent Scatter Radar (PFISR), *J. Atmos. Sol. Terr. Phys.*, *71*, 635, doi:10.1016/j.jastp.2009.01.009.

Knudsen, D. J., G. Haerendel, S. Buchert, M. C. Kelley, A. Steen, and U. Brandstrom (1993), Incoherent scatter radar spectrum distortions from intense auroral turbulence, *J. Geophys. Res.*, *98*, 9459–9471, doi:10.1029/93JA00179.

Lehtinen, M. S., and I. Häggström (1987), A new modulation principle for incoherent scatter measurements, *Radio Sci.*, *22*, 625–634, doi:10.1029/RS022i004p00625.

Lyons, L. R., E. Zesta, J. C. Samson, and G. D. Reeves (2000), Auroral disturbances during the January 10, 1997 magnetic storm, *Geophys. Res. Lett.*, *27*, 3237–3240, doi:10.1029/1999GL000014.

Lyons, L. R., I. O. Voronkov, E. F. Donovan, and E. Zesta (2002), Relation of substorm breakup arc to other growth-phase auroral arcs, *J. Geophys. Res.*, *107*(A11), 1390, doi:10.1029/2002JA009317.

Lyons, L. R., C.-P. Wang, M. Gkioulidou, and S. Zou (2009), Connections between plasma sheet transport, Region 2 currents, and entropy changes associated with convection, steady magnetospheric convection periods, and substorms, *J. Geophys. Res.*, *114*, A00D01, doi:10.1029/2008JA013743.

Lysak, R., and Y. Song (2002), Energetics of the ionospheric feedback interaction, *J. Geophys. Res.*, *107*(A8), 1160, doi:10.1029/2001JA000308.

Marklund, G. T. (1984), Auroral arc classification scheme based on the observed arc-associated electric field pattern, *Planet. Space Sci.*, *32*, 193–211, doi:10.1016/0032-0633(84)90154-5.

McPherron, R. L. (1972), Substorm related changes in the geomagnetic tail: The growth phase, *Planet. Space Sci.*, *20*, 1521–1539, doi:10.1016/0032-0633(72)90054-2.

Nicolls, M., and C. Heinselman (2007), Three-dimensional measurements of traveling ionospheric disturbances with the Poker Flat Incoherent Scatter Radar, *Geophys. Res. Lett.*, *34*, L21104, doi:10.1029/2007GL031506.

Nicolls, M. J., C. J. Heinselman, E. A. Hope, S. Ranjan, M. C. Kelley, and J. D. Kelly (2007), Imaging of Polar Mesosphere Summer Echoes with the 450 MHz Poker Flat Advanced Modular Incoherent Scatter Radar, *Geophys. Res. Lett.*, *34*, L20102, doi:10.1029/2007GL031476.

Picone, J. M., A. E. Hedin, D. P. Drob, and A. C. Aikin (2002), NRLMSISE-00 empirical model of the atmosphere: Statistical comparisons and scientific issues, *J. Geophys. Res.*, *107*(A12), 1468, doi:10.1029/2002JA009430.

Rostoker, G. (1999), The evolving concept of a magnetospheric substorm, *J. Atmos. Sol. Terr. Phys.*, *61*, 85–100, doi:10.1016/S1364-6826(98)00119-9.

Rostoker, G., S.-I. Akasofu, J. Foster, R. A. Greenwald, Y. Kamide, K. Kawasaki, A. T. Y. Lui, R. L. McPherron, and C. T. Russell (1980), Magnetospheric substorms: Definition and signatures, *J. Geophys. Res.*, *85*, 1663–1668, doi:10.1029/JA085iA04p01663.

Sato, T. (1978), A theory of quiet auroral arcs, *J. Geophys. Res.*, *83*, 1042–1048, doi:10.1029/JA083iA03p01042.

Schlegel, K., and D. R. Moorcroft (1989), EISCAT as a tristatic auroral radar, *J. Geophys. Res.*, *94*, 1430–1438.

Semeter, J., C. J. Heinselman, J. P. Thayer, R. A. Doe, and H. U. Frey (2003), Ion upflow enhanced by drifting F-region plasma structure along the nightside polar cap boundary, *Geophys. Res. Lett.*, *30*(22), 2139, doi:10.1029/2003GL017747.

Semeter, J., M. Zettergren, M. Diaz, and S. Mende (2008), Wave dispersion and the discrete aurora: New constraints derived from high-speed imagery, *J. Geophys. Res.*, *113*, A12208, doi:10.1029/2008JA013122.

Semeter, J., T. Butler, C. Heinselman, M. Nicolls, J. Kelly, and D. Hampton (2009), Volumetric imaging of the auroral ionosphere: Initial results from PFISR, *J. Atmos. Sol. Terr. Phys.*, *71*, 738–743, doi:10.1016/j.jastp.2008.08.014.

St.-Maurice, J.-P., C. Cussenot, and W. Kofman (1999), On the usefulness of E region electron temperatures and lower F region ion temperatures for the extraction of thermospheric parameters: A case study, *Ann. Geophys.*, *17*, 1182–1198, doi:10.1007/s00585-999-1182-2.

Sulzer, M. P., N. Aponte, and S. A. González (2005), Application of linear regularization methods to Arecibo vector velocities, *J. Geophys. Res.*, *110*, A10305, doi:10.1029/2005JA011042.

Tanaka, T. (2007), Magnetosphere-ionosphere convection as a compound system, *Space Sci. Rev.*, *133*, 1–72, doi:10.1007/s11214-007-9168-4.

Thayer, J. P. (1998), Height-resolved Joule heating rates in the high-latitude E region and the influence of neutral winds, *J. Geophys. Res.*, *103*, 471–487, doi:10.1029/97JA02536.

Wahlund, J.-E., H. Opgenoorth, I. Häggström, K. Winser, and G. Jones (1992), EISCAT observations of topside ionospheric ion outflows during auroral activity: Revisited, *J. Geophys. Res.*, *97*, 3019–3037, doi:10.1029/91JA02438.

Whalen, B. A., D. W. Green, and I. B. McDiarmid (1974), Observations of ionospheric ion flow and related convective electric fields in and near an auroral arc, *J. Geophys. Res.*, *79*, 2835–2842, doi:10.1029/JA079i019p02835.

Zettergren, M., J. Semeter, P.-L. Blelly, and M. Diaz (2007), Optical estimation of auroral ion upflow: Theory, *J. Geophys. Res.*, *112*, A12310, doi:10.1029/2007JA012691.

Zhu, P., J. Raeder, K. Germaschewski, and C. C. Hegna (2009), Initiation of ballooning instability in the near-Earth plasma sheet prior to the 23 March 2007 THEMIS substorm expansion onset, *Ann. Geophys.*, *27*, 1129–1138.

Zou, S., L. R. Lyons, C.-P. Wang, A. Boudouridis, J. M. Ruohoniemi, P. C. Anderson, P. L. Dyson, and J. C. Devlin (2009), On the coupling between the Harang reversal evolution and substorm dynamics: A synthesis of SuperDARN, DMSP, and IMAGE observations, *J. Geophys. Res.*, *114*, A01205, doi:10.1029/2008JA013449.

T. W. Butler and J. Semeter, Department of Electrical and Computer Engineering, Boston University, 8 Saint Mary's St., Boston, MA 02215, USA. (jls@bu.edu)

C. J. Heinselman and M. J. Nicolls, SRI International, 333 Ravenswood Ave., Menlo Park, CA 94025, USA.

M. Zettergren, Physical Sciences Department, Embry-Riddle Aeronautical University, 600 S. Clyde Morris Blvd., Daytona Beach, FL 32114, USA.